Terahertz detection based on nonlinear Hall effect without magnetic field

Yang Zhang[a] and Liang Fu[a,1]

[a]Department of Physics, Massachusetts Institute of Technology, Cambridge, MA 02139

Edited by Angel Rubio, Max Planck Institute for the Structure and Dynamics of Matter, Hamburg, Germany, and approved April 16, 2021 (received for review January 13, 2021)

We propose a method for broadband long-wavelength photodetection using the nonlinear Hall effect in noncentrosymmetric quantum materials. The inherently quadratic relation between transverse current and input voltage at zero magnetic field is used to rectify the incident terahertz or infrared electric field into a direct current, without invoking any diode. Our photodetector operates at zero external bias with fast response speed and has zero threshold voltage. Remarkably, the intrinsic current responsivity due to the Berry curvature mechanism is a material property independent of the incident frequency or the scattering rate, which can be evaluated from first-principles electronic structure calculations. We identify the Weyl semimetal NbP and ferroelectric semiconductor GeTe for terahertz/infrared photodetection with large current responsivity without external bias.

topological materials | terahertz | infrared | Berry curvature | nonlinear Hall effect

Quantum material is one of the most important fields in condensed-matter physics. While at a fundamental level the properties of all materials are governed by quantum mechanics, quantum materials are distinctive in that they exhibit novel electrical and optical properties originating from the quantum nature of electron wavefunction. The complexity and richness of quantum wavefunction underlie new phases of matter and emergent properties, as revealed through the lens of geometry (1), topology (2), and entanglement (3). The rise of quantum materials not only advances our fundamental understanding of solids but also opens exciting opportunities for inventing new technologies.

Terahertz technology is a fast-growing field with wide-ranging applications (4, 5). Since terahertz waves can transmit through many materials, terahertz spectroscopy and imaging can be used to identify concealed objects for security check, detect chemical composition and material defects for quality control, and examine biological tissues in medical imaging. Terahertz sensors can help autonomous vehicles to identify remote objects under foggy conditions. Terahertz-band communication is regarded as a key enabling technology for the next-generation wireless networks. Despite the enormous potential, fast, sensitive, and broadband terahertz detection at room temperature has been a technology challenge. Conventional terahertz detectors, such as Golay cells, bolometers, and pyroelectric sensors, rely on thermal response and therefore usually require cryogenic cooling and have slow operation speed. Alternatively, Schottky diodes in conjunction with antennas are used to convert high-frequency electric field signals to direct current (DC). However, they typically have cutoff frequencies below 1 THz.

In this work, we propose a method of terahertz detection based on the intrinsic nonlinear Hall effect in quantum materials. This effect was predicted (6) and observed (7, 8) in inversion-breaking crystals without the need of magnetic field, where an applied electric field induces a transverse current to the second order (9, 10). Our idea here is to use this quadratic transverse current–voltage characteristic of quantum materials to rectify and detect terahertz radiation directly, without invoking any junction region. This "Hall rectifier" (11) has a number of important advantages. It is an intrinsic full-wave rectifier with a large attainable responsivity at zero bias and a high cutoff frequency that ranges from subterahertz to tens of terahertz. It features a very short response time down to ps. Due to its simple device architecture, Hall rectifiers can be easily fabricated, integrated on chip, and potentially mass produced.

Remarkably, we show that the current responsivity due to the intrinsic second-order Hall effect is independent of the frequency and intensity of incident radiation, and it is an intrinsic material property determined by electronic band structure and the Berry curvature dipole (6). This finding enables us to predict the right materials for high-sensitivity terahertz detection using first-principles calculations. We identify a number of topological semimetals with anisotropic energy dispersion, in which the intrinsic current responsivity can reach 1 A/W without external bias and over a very broad range of frequency.

Unlike photogalvanic effects at optical frequencies due to interband transitions (12–26), the photoresponse of metals and degenerate semiconductors in the terahertz frequency range is usually governed by an intraband process involving electrons near the Fermi surface only. Importantly, since the dispersion relation of the Bloch electron in nonmagnetic materials necessarily satisfies $\epsilon_{\boldsymbol{k}} = \epsilon_{-\boldsymbol{k}}$ due to time-reversal symmetry, the second-order response of noncentrosymmetric materials is an inherently quantum-mechanical effect arising from the inversion asymmetry of the electron wavefunction within the unit cell. Therefore, quantum materials having complex Bloch wavefunctions, such as topological surface states and inversion-breaking topological metals, generally exhibit a large second-order response.

Significance

Despite the enormous potential of terahertz technology, fast, sensitive, and broadband terahertz detection at room temperature has been a challenge. We propose a method for long-wavelength photodetection using topological quantum materials without invoking any diode or junction region. The inherently quadratic relation between transverse current and input voltage at zero magnetic field is used to rectify the incident terahertz or infrared electric field into a direct current. We identify the Weyl semimetal NbP and ferroelectric semiconductor GeTe for terahertz/infrared photodetection with large current responsivity without external bias.

Author contributions: L.F. designed research; Y.Z. and L.F. performed research; Y.Z. and L.F. analyzed data; and L.F. wrote the main text with inputs from Y.Z.

The authors declare no competing interest.

This article is a PNAS Direct Submission.

[1]To whom correspondence may be addressed. Email: liangfu@mit.edu.

This article contains supporting information online at https://www.pnas.org/lookup/suppl/doi:10.1073/pnas.2100736118/-/DCSupplemental.

Published May 17, 2021.

We start with a brief review of the nonlinear Hall effect due to the Berry curvature dipole (6). As a type of second-order response, this effect can be viewed as a current-induced anomalous Hall effect. The anomalous current due to Berry curvature $\mathbf{\Omega_k}$ is given by

$$\mathbf{j}^A = \frac{e^2}{\hbar}\int \frac{d^d\mathbf{k}}{(2\pi)^d} f(\mathbf{k})\,(\mathbf{E}\times\mathbf{\Omega_k}), \qquad [1]$$

where E is the applied electric field and $f(\mathbf{k})$ is the distribution function in the presence of the field. To first order in E, the anomalous current is obtained by replacing f with the equilibrium Fermi–Dirac distribution $f^0(\mathbf{k}) = 1/(e^{\beta(\epsilon_\mathbf{k}-\mu)}+1)$. In time-reversal-invariant and inversion-breaking systems, Berry curvature can be nonzero, but the condition $\mathbf{\Omega_k} = -\mathbf{\Omega}_{-\mathbf{k}}$ leads to zero linear-response anomalous current due to the cancellation of contributions from Bloch electrons at $\pm\mathbf{k}$.

On the other hand, the anomalous current can be nonzero when we extend the analysis to the second order in E. In the current-carrying state, the distribution function f differs from equilibrium and, to first order in E, is given by

$$f(\mathbf{k}) = f^0(\mathbf{k}) + \frac{e\mathbf{E}\tau}{\hbar}\cdot(\partial_\mathbf{k} f^0), \qquad [2]$$

where τ is the scattering rate in Drude transport. Then, the anomalous current at second order is obtained as

$$j_a^A = \left(\epsilon_{ab\lambda}\frac{e^3\tau B_{\lambda c}}{\hbar^2}\right)E_b E_c \equiv \chi_{abc} E_b E_c, \qquad [3]$$

where the nonlinear Hall conductivity χ_{abc} is a third-rank tensor that is antisymmetric in indexes a, b. $B_{\lambda c}$ is the Berry curvature dipole, an intrinsic property of Bloch electron wavefunctions defined by ref. 6:

$$B_{\lambda c} = \int \frac{d^d\mathbf{k}}{(2\pi)^d} f^0(\mathbf{k})\frac{\partial\Omega_\lambda}{\partial k_c}. \qquad [4]$$

B is allowed by symmetry in noncentrosymmetric crystals and surfaces having certain point groups (see below). For example, in materials with a polar axis, large B has been found due to the presence of tilted Dirac or Weyl points in the band structure (6, 27–35). When B is nonzero and in the presence of an applied electric field, the imbalance in the probability of occupation $f(\mathbf{k}) \neq f(-\mathbf{k})$ leads to a net Berry curvature, which then induces a second-order anomalous current in the transverse direction.

The inherently quadratic relation between the transverse current and input voltage due to the nonlinear Hall effect is ideal for rectifying alternating current (AC) input $\mathbf{E}(t) = \mathbf{E}\cos(\omega t)$, including both the positive and negative half cycles. At very low frequency $\omega \ll 1/\tau$, the time-dependent transverse current simply follows the AC voltage, $j^A(t) = j^A|_{E(t)} \propto \cos^2(\omega t)$, which is a sum of DC and 2ω components with equal weight. Thus, the DC output j^0, or the time average of $j^A(t)$ over a full cycle, is given by $j^0 = \frac{1}{2}j^A = \frac{1}{2}\chi EE$. Unlike diodes, our Hall rectifier does not involve any junction or barrier structure, but relies on the inherent nonlinearity of a homogeneous quantum material. Since the carriers do not need to overcome a barrier to conduct a current, the Hall rectifier has a zero-threshold voltage and operates without the need of a finite bias, which is ideally suited for detecting small signals in terahertz frequency. Since both positive and negative voltages generate transverse current in the same direction, dark current is eliminated.

Provided that the incident frequency is well below the threshold for interband transition, the second-order direct current due to the Berry curvature mechanism shows a Drude-like response (6, 9, 10)

$$j_a^0 = \left(\frac{1}{1+\omega^2\tau^2}\right)\frac{\chi_{abc}}{2}E_b E_c, \qquad [5]$$

where the frequency dependence comes from the change of distribution function to the first order of the oscillating electric field. Note that for time-reversal-invariant systems, the DC photocurrent effect and, more generally, the linear photogalvanic effect vanishes in the absence of dissipation $\tau^{-1}\to 0$, because time-reversal symmetry forbids a direct current (37). At frequencies $\omega \gg \tau^{-1}$, the photocurrent j^0 from the intraband process decreases as $1/\omega^2$. However, in reality, even in the case of good metals, the scattering rate at room temperature is at least a few tens of terahertz. Therefore, the nonlinear Hall effect of a homogeneous quantum material can be used as a replacement of diodes to rectify incident waves in a very broad range of frequency up to at least 10 THz, and the output direct current is linearly proportional to the incident power.

An important parameter for terahertz detectors is current responsivity, which measures the electrical output per optical input. In our device shown in Fig. 1, the antennas collect the incident radiation and create a strongly enhanced terahertz field in the active region of the Hall rectifier, which generates the photoresponse current in the transverse direction. The power absorbed by the Hall rectifier $P = \sigma_{ab}(\omega)E_a E_b S$, where $S = LW$ is the area of the Hall rectifier with length L and width W. σ is the linear-response AC conductivity given by

$$\sigma_{ab}(\omega) = \frac{e^2 D_{ab}}{\hbar^2}\frac{\tau}{(1+\omega^2\tau^2)} \qquad [6]$$

within Drude transport theory, where the Drude weight D is defined by

$$D_{ab} = \int \frac{d^d k}{(2\pi)^d}\frac{\partial E}{\partial k_a}\frac{\partial E}{\partial k_b}\left(-\frac{\partial f_0}{\partial E}\right). \qquad [7]$$

The output current per absorbed power defines the current responsivity of our Hall rectifier:

$$R = \frac{I_H}{P} = \frac{1}{W}\frac{j^0}{\sigma_{ab}E_a E_b}. \qquad [8]$$

Note that R is inversely proportional to the width of the Hall rectifier, so it is advantageous to use a narrow channel.

Due to the quadratic dependence of transverse current j^0 on the terahertz field, R is inherently independent of incident power; i.e., our terahertz detector exhibits ideal linearity over a large range of optical power. Moreover, since both the nonlinear Hall conductivity and linear response conductivity exhibit Drude behavior with the same $\tau/(1+\omega^2\tau^2)$ dependence, R is independent of frequency and scattering rate, regardless of the value of $\omega\tau$. Therefore, the current responsivity due to the intrinsic nonlinear Hall effect is entirely determined by the Berry curvature dipole B and the Drude weight D. B is a property of Bloch electron wavefunction, and D is a property of energy dispersion. This is an important result of our work. As both B and D are material properties attainable from first-principles electronic structure calculations, the intrinsic current responsivity R of quantum materials can be predicted without any tuning parameter. This enables computational materials design of long-wavelength photodetectors.

Concerning practical application, the responsivity of a photodetector measures the electrical output per incident optical power, which is reduced from the intrinsic responsivity R defined above by the absorption coefficient, i.e., the ratio

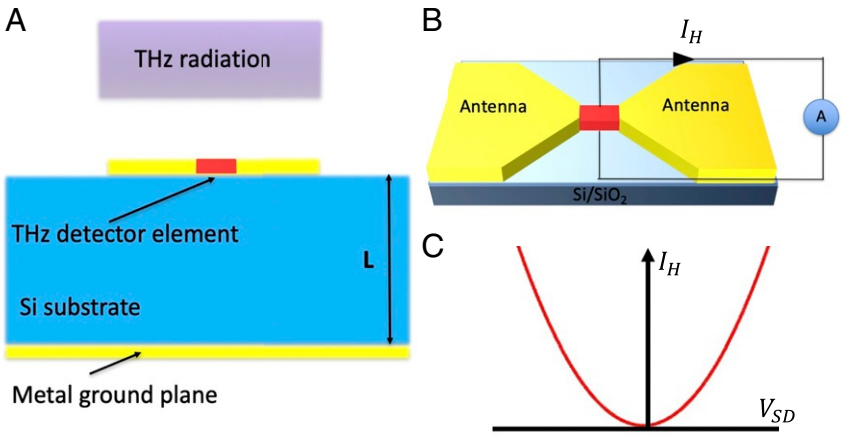

Fig. 1. Terahertz photodetection based on the nonlinear Hall effect in quantum materials. (*A*) Schematic diagram of an antenna-coupled topological semimetal or ferroelectric semiconductor terahertz detector element with substrate resonant cavity length of L. The thickness of substrate is given by the resonant condition $L = \frac{2n+1}{4\sqrt{\varepsilon_r}}\lambda_0$ $(n = 0, 1, 2\ldots)$ with ε_r as the dielectric constant of the Si substrate and λ_0 as the wavelength of incoming terahertz radiation in free space (36). (*B*) The oscillating terahertz field enhanced by a bowtie antenna induces a direct current in the transverse direction via the intrinsic second-order response of the quantum material itself. (*C*) Current–voltage characteristic of the nonlinear Hall rectifier. The quadratic relation enables full-wave rectification of AC input at zero external bias, with zero threshold voltage and zero dark current.

between absorbed and incident power. Resonant optical cavity and antenna with impedance match (Fig.1) can be used to maximize the absorption of incident terahertz radiation and optimize the photodetector responsivity toward the fundamental limit R set by the intrinsic second-order nonlinearity of quantum materials.

To search for quantum materials suitable for the Hall rectifier, we note that a large Berry curvature dipole appears in the vicinity of band crossings with anisotropic energy dispersion. Therefore inversion-breaking Weyl semimetals such as TaAs, TaP, NbP, and NbAs (38–41) are good candidates. Our first-principles calculations reveal that among these four materials, NbP has the largest current responsivity (Fig. 2). The NbP family of Weyl semimetals has the point group C_{4v} with a fourfold rotation axis in the z direction and two vertical mirror planes $\mathcal{M}_x$, $\mathcal{M}_y$. Thus, the only nonzero elements of the Berry curvature dipole tensor are $B_{yx} = -B_{xy}$. Hence, the photoresponse is largest when the incident electric field lies within the xy plane and the photocurrent along the z direction is measured. In this configuration, the intrinsic current responsivity is given by

$$R = \frac{1}{W}\frac{eB_{xy}}{2D_{xx}}. \qquad [9]$$

Interestingly, we find that large contributions to the Berry curvature dipole in NbP come from regions near two extended loops in momentum space, rather than the vicinity of Weyl points as in TaAs. These loops are located on a $\mathcal{M}_x$-invariant plane and correspond to a nodal line of band crossings that would occur due to band inversion if spin–orbit coupling were turned off.

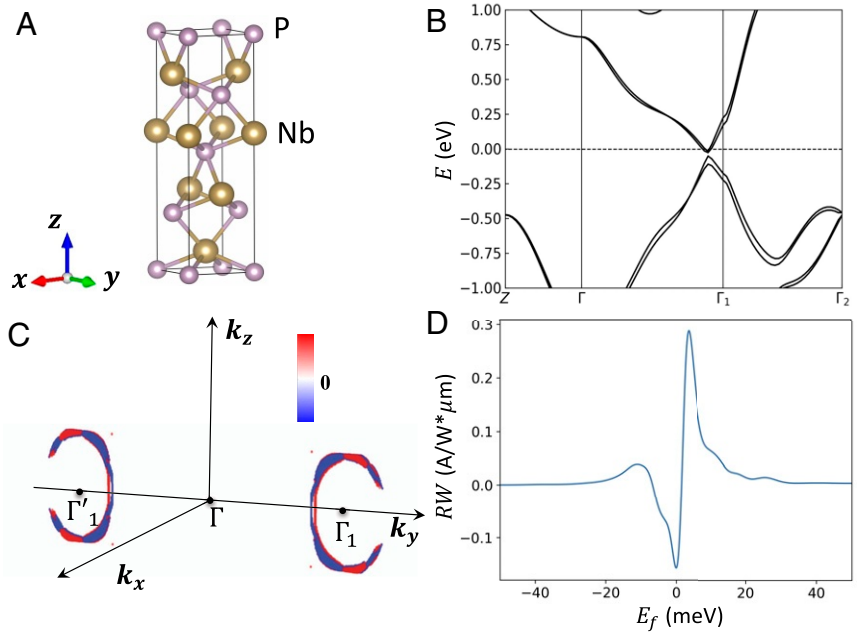

Fig. 2. (*A*) Lattice structure of NbP. (*B*) Band structure of NbP, which shows a narrow band inversion around Γ_1. (*C*) Three-dimensional momentum resolved Berry curvature dipole. (*D*) Current responsivity as a function of chemical potential.

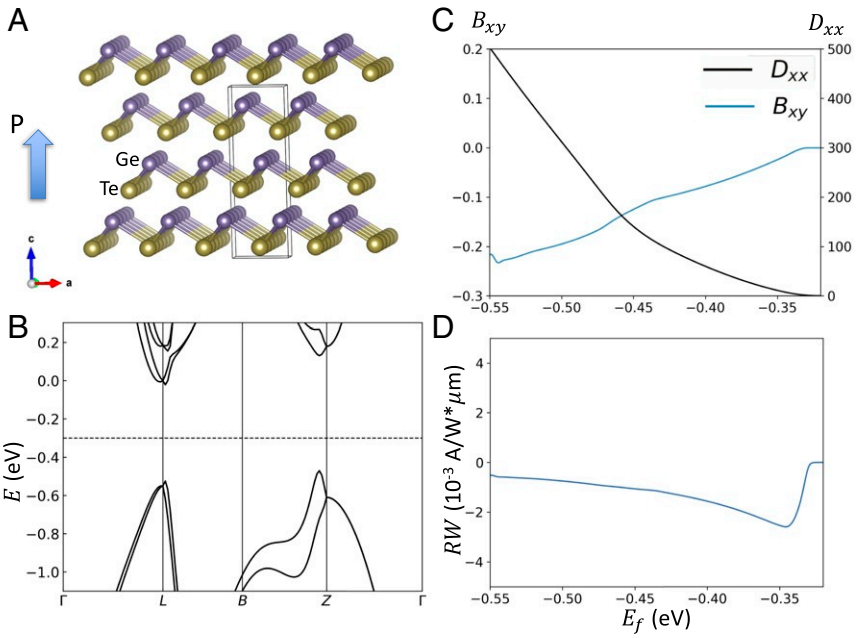

Fig. 3. (*A*) Schematic illustration of rhombohedral distorted rock salt crystal structure of ferroelectric semiconductor GeTe with polarization along the *c* axis. (*B*) Fully relativistic band structure of GeTe along high-symmetry lines. The dotted line stands for the Fermi level at −0.3 eV. (*C*) Chemical potential-dependent Berry curvature dipole B_{xy} and Drude weight D_{xx} (in the unit of $\frac{\hbar V}{e}(\Omega\text{cm})^{-1}$). (*D*) current responsivity as a function of chemical potential in the valence band side of GeTe.

The introduction of spin–orbit coupling leads to strong momentum-dependent band hybridization and therefore creates anisotropic energy dispersion and a large Berry curvature dipole near the Fermi level. As a result, a large current responsivity R is found for a range of Fermi energy within ± 20 meV. Our calculation shows that the responsivity of the NbP-based long-wavelength photodetector at zero external bias can reach about 0.3 A/W for a realistic device width $W = 1$ μm. Reducing the width to $W = 0.1$ μm leads to $R = 3$ A/W.

We further calculate the current responsivity for other type I Weyl semimetal TaAs, TaP, and NbAs with point group C_{4v} (NbAs shows a similar magnitude to NbP; see *SI Appendix* for details) and type II Weyl semimetal $MoTe_2$ and WTe_2 with point group C_{2v}. In general, type I Weyl semimetals have a larger current responsivity because of the reduced Drude weight from small electron (hole) pockets.

Besides the topological semimetal, ferroelectric semiconductors are also promising candidates where the current responsivity can be optimized by doping. The ferroelectric XTe (X = Ge, Sn) monochalcogenides share rhombohedrally distorted rock salt structure (space group R3m). In particular, GeTe has a remarkably high Curie temperature up to 700 K. Here we calculate the Berry curvature dipole and current responsivity in p-doped GeTe. While the global bandgap of GeTe is 0.32 eV, the Berry curvature dipole B_{xy} reaches 0.5, which is much larger than that of the Rashba semiconductor BiTeI at the topological phase transition (30). As shown in Fig. 3, the resulting current responsivity of GeTe is sizable over a wide range of doping, which is attractive for room-temperature terahertz photodetection.

All of the materials identified here possess a polar axis. To use these materials for terahertz detection, it is important to consider the orientation of the polar axis. When the polar axis lies within the plane, terahertz radiation at normal incidence will produce a photocurrent along the polar axis. When the polar axis is out of plane (z axis), there is no in-plane photocurrent with normal incidence. However, the nonlinear Hall effect from the Berry curvature dipole results in $\chi_{xzx} = -\chi_{zxx}$ and $\chi_{yzy} = -\chi_{zyy}$, so that terahertz radiation at oblique incidence will produce an in-plane photocurrent, which enables photodetection in the device configuration shown in Fig. 1.

In Fig. 4, we compare the performance of our nonlinear Hall long-wavelength photodetector with that of other detectors and rectifiers. To this end, we plot their current responsivity versus operating frequency (42–53). In the long-wavelength region below 37 THz, the current responsivity is typically limited to less than 1 A/W and varies dramatically with operating frequency. As the Drude half-width of NbP at room temperature determined from optical conductivity is around 30 meV (54), we expect our nonlinear Hall photodetector can operate up to 15 THz with a large current responsivity reaching 3 A/W. At higher frequency, the interband linear photogalvanic effect (LGPE) starts to dominate in the TaAs family of Weyl semimetals (21, 55). As shown

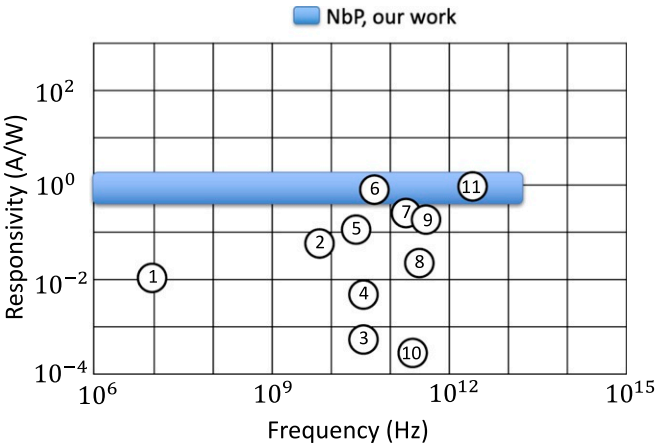

Fig. 4. Comparison of current responsivity to that in previous studies in the frequency range 10^6 to 10^{15} Hz. The reference data points are adopted and updated from a terahertz detector review article (42); labels 1 to 11 correspond to a series of works on two-dimensional materials and topological semimetals (43–53).

in *SI Appendix*, we find a large current responsivity due to LGPE for TaAs, NbP, and GeTe, which provides a promising platform for infrared photodetection.

Another important figure of merit for photodetection is the noise-equivalent power (NEP), defined as the noise power density over the responsivity. At room temperature, thermal noise is the dominant noise source compared to the shot noise from discrete incident photons. We compute the NEP from the root-mean square of the noise current as $NEP = \frac{\sqrt{4k_B T/r_0}}{R}$, where T is the operating temperature and r_0 is the sample resistance. With sample width $W = 0.1\mu$m and room temperature resistance $r_0 = 300\ \Omega$ (56), the NEP of the NbP device at peak responsivity is estimated to be 2.5 pW/Hz$^{0.5}$. For comparison, the NEP of the typical Schottky diode-based terahertz detector is around 100 pW/Hz$^{0.5}$ at the subterahertz ($0.1 \sim 1$ THz) range and quickly increases at the higher frequency.

In addition to the Berry curvature dipole, other mechanisms including skew scattering and side jump also contribute to the nonlinear Hall effect (10, 11, 57–63). For crystals with certain point groups such as C_{3v}, although the Berry curvature dipole cannot contribute to the in-plane nonlinear Hall effect, theory predicts that second-order nonlinear transport in diffusive systems arises from skew scattering and side jump induced by the inherent chirality of Bloch electron wavefunction (11). Moreover, in the ballistic transport regime, nonlinear Hall conductance is entirely determined by the integral of Berry curvature over half of the Fermi surface (64), which is also an intrinsic property of Bloch electron wavefunction. Regardless of the microscopic origins, the inherent second-order nonlinearity of quantum materials can be utilized for long-wavelength photodetection by rectifying oscillating electric field into direct current.

On the experimental side, a second-order response was observed in recent electrical transport (65) and terahertz photocurrent experiments (66, 67) on topological insulators. This effect arises from the Dirac surface states with hexagonal warping (68), which enables second-order response due to Berry curvature and skew scattering. The dependence of photocurrent on incident frequency between 0.5 and 4 THz is consistent with Drude behavior expected from intraband processes. Very recently, a nonlinear Hall effect at room temperature was observed in type II Weyl semimetal $TaIrTe_4$ and enabled radiofrequency rectification (69). Moreover, room temperature terahertz detection and imaging have been achieved using the second-order nonlinear response of topological surface states in Dirac semimetal $PdTe_2$ (49). The photocurrent as a function of incident power displays excellent linearity. Remarkably, the current responsivity without bias reaches as large as 0.2 A/W. These exciting results on many fronts encourage future development of terahertz/infrared technology based on Hall rectifiers.

Methods

For TaAs, TaP, NbAs, NbP, $MoTe_2$, WTe_2, and GeTe, we first perform density functional theory (DFT) Bloch wave functions from the full-potential local-orbital (FPLO) program (70) within the generalized gradient approximation (GGA) (71). By projecting the Bloch wavefunction to localized Wannier functions, we construct the tight-binding model with 40 bands from *d* and *s* orbitals for transition metal Nb (Ta) and *s* and *p* orbitals for pnicogen P (As). For $MoTe_2$ and WTe_2, the tight-binding model is constructed with 88 bands from *d* orbitals for Mo (W) and *p* orbitals for Te. For ferroelectric GeTe, the tight-binding model is constructed with 52 bands from 4*s*, 4*p*, 5*s*, 5*p*, 4*d* orbitals for Ge and 5*s*, 5*p*, 6*s*, 5*d*, 6*p* orbitals for Te as the tight-binding model with reduced basis has a large error fitting to the DFT band structure. The Berry curvature dipole and Drude conductivity integration are both done with a $500 \times 500 \times 500$ momentum space mesh.

Data Availability. All study data are included in this article and/or *SI Appendix*.

ACKNOWLEDGMENTS. This work was supported by the US Army Research Laboratory and the US Army Research Office through the Institute for Soldier Nanotechnologies, under Collaborative Agreement W911NF-18-2-0048. Y.Z. and L.F. were supported in part by a Simons Investigator Award from the Simons Foundation.

1. N. Nagaosa, J. Sinova, S. Onoda, A. H. MacDonald, N. P. Ong, Anomalous Hall effect. *Rev. Mod. Phys.* **82**, 1539 (2010).
2. M. Z. Hasan, C. L. Kane, Colloquium: Topological insulators. *Rev. Mod. Phys.* **82**, 3045 (2010).
3. L. Savary, L. Balents, Quantum spin liquids: A review. *Rep. Prog. Phys.* **80**, 016502 (2016).
4. M. Tonouchi, Cutting-edge terahertz technology. *Nat. Photonics* **1**, 97–105 (2007).
5. F. Sizov, A. Rogalski, THz detectors. *Prog. Quant. Electron.* **34**, 278–347 (2010).
6. I. Sodemann, L. Fu, Quantum nonlinear Hall effect induced by Berry curvature dipole in time-reversal invariant materials. *Phys. Rev. Lett.* **115**, 216806 (2015).
7. Q. Ma *et al.*, Observation of the nonlinear Hall effect under time-reversal-symmetric conditions. *Nature* **565**, 337–342 (2019).
8. K. Kang, T. Li, E. Sohn, J. Shan, K. F. Mak, Observation of the nonlinear anomalous Hall effect in 2d wte2. Nonlinear anomalous Hall effect in few-layer WTe2. *Nat. Mater.* **18**, 324–328 (2019).
9. J. E. Moore, J. Orenstein, Confinement-induced Berry phase and helicity-dependent photocurrents. *Phys. Rev. Lett.* **105**, 026805 (2010).
10. E. Deyo, L. Golub, E. Ivchenko, B. Spivak, Semiclassical theory of the photogalvanic effect in non-centrosymmetric systems. arXiv [Preprint] (2009). https://arxiv.org/abs/0904.1917 (Accessed 14 March 2021).
11. H. Isobe, S. Y. Xu, L. Fu, High-frequency rectification via chiral Bloch electrons. *Sci. Adv.* **6**, eaay2497 (2020).
12. J. Sipe, A. Shkrebtii, Second-order optical response in semiconductors. *Phys. Rev. B* **61**, 5337 (2000).
13. F. de Juan, A. G. Grushin, T. Morimoto, J. E. Moore, Quantized circular photogalvanic effect in Weyl semimetals. *Nat. Commun.* **8**, 1–7 (2017).
14. T. Morimoto, N. Nagaosa, Topological nature of nonlinear optical effects in solids. *Sci. Adv.* **2**, e1501524 (2016).
15. C. K. Chan, P. A. Lee, K. S. Burch, J. H. Han, Y. Ran, When chiral photons meet chiral fermions: Photoinduced anomalous Hall effects in Weyl semimetals. *Phys. Rev. Lett.* **116**, 026805 (2016).
16. H. Ishizuka, T. Hayata, M. Ueda, N. Nagaosa, Emergent electromagnetic induction and adiabatic charge pumping in noncentrosymmetric Weyl semimetals. *Phys. Rev. Lett.* **117**, 216601 (2016).
17. X. Yang, K. Burch, Y. Ran, Divergent bulk photovoltaic effect in Weyl semimetals. arXiv [Preprint] (2017). https://arxiv.org/abs/1712.09363 (Accessed 14 March 2021).
18. S. M. Young, A. M. Rappe, First principles calculation of the shift current photovoltaic effect in ferroelectrics. *Phys. Rev. Lett.* **109**, 116601 (2012).
19. D. E. Parker, T. Morimoto, J. Orenstein, J. E. Moore, Diagrammatic approach to nonlinear optical response with application to Weyl semimetals. *Phys. Rev. B* **99**, 045121 (2019).
20. S. Y. Xu *et al.*, Electrically switchable Berry curvature dipole in the monolayer topological insulator wte 2. *Nat. Phys.* **14**, 900–906 (2018).
21. G. B. Osterhoudt *et al.*, Colossal mid-infrared bulk photovoltaic effect in a type-I Weyl semimetal. *Nat. Mater.* **18**, 471–475 (2019).
22. D. Rees *et al.*, Helicity-dependent photocurrents in the chiral Weyl semimetal RhSi. *Sci. Adv.* **6**, eaba0509 (2020).
23. Z. Ni *et al.*, Giant topological longitudinal circular photo-galvanic effect in the chiral multifold semimetal CoSi. *Nat. Commun.* **12**, 154 (2021).
24. J. Ma *et al.*, Nonlinear photoresponse of type-II Weyl semimetals. *Nat. Mater.* **18**, 476–481 (2019).
25. Q. Ma *et al.*, Direct optical detection of Weyl fermion chirality in a topological semimetal. *Nat. Phys.* **13**, 842–847 (2017).
26. E. König, H. Y. Xie, D. Pesin, A. Levchenko, Photogalvanic effect in Weyl semimetals. *Phys. Rev. B* **96**, 075123 (2017).
27. Y. Zhang, Y. Sun, B. Yan, Berry curvature dipole in Weyl semimetal materials: An ab initio study. *Phys. Rev. B* **97**, 041101 (2018).
28. S. Dzsaber *et al.*, Giant spontaneous Hall effect in a nonmagnetic Weyl-Kondo semimetal. arXiv [Preprint] (2018). https://arxiv.org/abs/1811.02819 (Accessed 14 March 2021).
29. Y. Zhang, J. Van Den Brink, C. Felser, B. Yan, Electrically tuneable nonlinear anomalous Hall effect in two-dimensional transition-metal dichalcogenides WTe2 and MoTe2. *2D Mater.* **5**, 044001 (2018).
30. J. I. Facio *et al.*, Strongly enhanced Berry dipole at topological phase transitions in BiTeI. *Phys. Rev. Lett.* **121**, 246403 (2018).
31. J. S. You, S. Fang, S. Y. Xu, E. Kaxiras, T. Low, Berry curvature dipole current in the transition metal dichalcogenides family. *Phys. Rev. B* **98**, 121109 (2018).
32. J. Son, K. H. Kim, Y. Ahn, H. W. Lee, J. Lee, Strain engineering of the Berry curvature dipole and valley magnetization in monolayer MoS_2. *Phys. Rev. Lett.* **123**, 036806 (2019).
33. B. T. Zhou, C. P. Zhang, K. T. Law, Highly tunable nonlinear Hall effects induced by spin-orbit couplings in strained polar transition-metal dichalcogenides. *Phys. Rev. Appl.* **13**, 024053 (2020).

34. P. A. Pantaleon, T. Low, F. Guinea, Tunable large Berry dipole in strained twisted bilayer graphene. arXiv [Preprint] (2020). https://arxiv.org/abs/2010.11086 (Accessed 14 March 2021).
35. S. S. Tsirkin, P. A. Puente, I. Souza, Gyrotropic effects in trigonal tellurium studied from first principles. *Phys. Rev. B* **97**, 035158 (2018).
36. X. Tu *et al.*, Investigation of antenna-coupled Nb_5N_6 microbolometer THz detector with substrate resonant cavity. *Opt. Express.* **26**, 8990–8997 (2018).
37. T. Morimoto, N. Nagaosa, Nonreciprocal current from electron interactions in noncentrosymmetric crystals: Roles of time reversal symmetry and dissipation. *Sci. Rep.* **8**, 1–16 (2018).
38. A. Bansil, H. Lin, T. Das, Colloquium: Topological band theory. *Rev. Mod. Phys.* **88**, 021004 (2016).
39. M. Z. Hasan, S. Y. Xu, I. Belopolski, S. M. Huang, Discovery of Weyl fermion semimetals and topological Fermi arc states. *Annu. Rev. Condens. Matter Phys.* **8**, 289–309 (2017).
40. H. Weng, C. Fang, Z. Fang, B. A. Bernevig, X. Dai, Weyl semimetal phase in noncentrosymmetric transition-metal monophosphides. *Phys. Rev. X* **5**, 011029 (2015).
41. N. Armitage, E. Mele, A. Vishwanath, Weyl and Dirac semimetals in three-dimensional solids. *Rev. Mod. Phys.* **90**, 015001 (2018).
42. A. Rogalski, M. Kopytko, P. Martyniuk, Two-dimensional infrared and terahertz detectors: Outlook and status. *Appl. Phys. Rev.* **6**, 021316 (2019).
43. Y. Yao *et al.*, High-responsivity mid-infrared graphene detectors with antenna-enhanced photocarrier generation and collection. *Nano Lett.* **14**, 3749–3754 (2014).
44. A. Pospischil *et al.*, Cmos-compatible graphene photodetector covering all optical communication bands. *Nat. Photonics* **7**, 892–896 (2013).
45. F. Xia, T. Mueller, Ym. Lin, A. Valdes-Garcia, P. Avouris, Ultrafast graphene photodetector. *Nat. Nanotechnol.* **4**, 839–843 (2009).
46. D. Schall *et al.*, 50 Gbit/s photodetectors based on wafer-scale graphene for integrated silicon photonic communication systems. *ACS Photonics* **1**, 781–784 (2014).
47. X. Gan *et al.*, Chip-integrated ultrafast graphene photodetector with high responsivity. *Nat. Photonics* **7**, 883–887 (2013).
48. S. Cakmakyapan, P. K. Lu, A. Navabi, M. Jarrahi, Gold-patched graphene nanostripes for high-responsivity and ultrafast photodetection from the visible to infrared regime. *Light Sci. Appl.* **7**, 1–9 (2018).
49. C. Guo *et al.*, Anisotropic ultrasensitive PdTe2-based phototransistor for room-temperature long-wavelength detection. *Sci. Adv.* **6**, eabb6500 (2020).
50. G. Auton *et al.*, Terahertz detection and imaging using graphene ballistic rectifiers. *Nano Lett.* **17**, 7015–7020 (2017).
51. L. Viti *et al.*, Plasma-wave terahertz detection mediated by topological insulators surface states. *Nano Lett.* **16**, 80–87 (2016).
52. L. Viti *et al.*, Black phosphorus terahertz photodetectors. *Adv. Mater.* **27**, 5567–5572 (2015).
53. D. A. Bandurin *et al.*, Resonant terahertz detection using graphene plasmons. *Nat. Commun.* **9**, 5392 (2018).
54. D. Neubauer *et al.*, Optical conductivity of the Weyl semimetal NbP. *Phys. Rev. B* **98**, 195203 (2018).
55. Y. Zhang *et al.*, Photogalvanic effect in Weyl semimetals from first principles. *Phys. Rev. B* **97**, 241118 (2018).
56. C. Shekhar *et al.*, Extremely large magnetoresistance and ultrahigh mobility in the topological Weyl semimetal candidate NbP. *Nat. Phys.* **11**, 645–649 (2015).
57. Z. Du, C. Wang, S. Li, H. Z. Lu, X. Xie, Disorder-induced nonlinear Hall effect with time-reversal symmetry. *Nat. Commun.* **10**, 1–6 (2019).
58. Z. Du, C. Wang, H. P. Sun, H. Z. Lu, X. Xie, Quantum theory of the nonlinear Hall effect. arXiv [Preprint] (2020). https://arxiv.org/abs/2004.09742 (Accessed 14 March 2021).
59. C. Xiao, Z. Du, Q. Niu, Theory of nonlinear Hall effects: Modified semiclassics from quantum kinetics. *Phys. Rev. B* **100**, 165422 (2019).
60. C. Xiao, H. Zhou, Q. Niu, Scaling parameters in anomalous and nonlinear Hall effects depend on temperature. *Phys. Rev. B* **100**, 161403 (2019).
61. L. Golub, E. Ivchenko, B. Spivak, Semiclassical theory of the circular photogalvanic effect in gyrotropic systems. *Phys. Rev. B* **102**, 085202 (2020).
62. O. Matsyshyn, I. Sodemann, Nonlinear Hall acceleration and the quantum rectification sum rule. *Phys. Rev. Lett.* **123**, 246602 (2019).
63. M. S. Rudner, J. C. Song, Self-induced Berry flux and spontaneous non-equilibrium magnetism. *Nat. Phys.* **15**, 1017–1021 (2019).
64. M. Papaj, L. Fu, Magnus Hall effect. *Phys. Rev. Lett.* **123**, 216802 (2019).
65. P. He *et al.*, Quantum frequency doubling in the topological insulator Bi2Se3. *Nat Commun.* **12**, 698 (2021).
66. P. Olbrich *et al.*, Room-temperature high-frequency transport of Dirac fermions in epitaxially grown Sb2Te3- and Bi2Te3-based topological insulators. *Phys. Rev. Lett.* **113**, 096601 (2014).
67. H. Plank *et al.*, Photon drag effect in $(Bi_{1-x}Sbx)_2Te_3$ three-dimensional topological insulators. *Phys. Rev. B* **93**, 125434 (2016).
68. L. Fu, Hexagonal warping effects in the surface states of the topological insulator Bi2Te3. *Phys. Rev. Lett.* **103**, 266801 (2009).
69. D. Kumar *et al.*, Room-temperature nonlinear Hall effect and wireless radiofrequency rectification in Weyl semimetal TaIrTe4. *Nat. Nanotechnol.* **16**, 421–425 (2021).
70. K. Koepernik, H. Eschrig, Full-potential nonorthogonal local-orbital minimum-basis band-structure scheme. *Phys. Rev. B* **59**, 1743 (1999).
71. J. P. Perdew, K. Burke, M. Ernzerhof, Generalized gradient approximation made simple. *Phys. Rev. Lett.* **77**, 3865 (1996).